

Northumbria Research Link

Citation: Qu, Yuwei, Yuan, Jinhui, Qiu, Shi, Zhou, Xian, Yan, Binbin, Wu, Qiang, Liu, Bin, Wang, Kuiru, Sang, Xinzhu, Long, Keping and Yu, Chongxiu (2021) Simple structure dual-core photonic crystal fiber polarization beam splitter covering the O + E + S + C + L + U band based on the surface plasmon resonance effect. Journal of the Optical Society of America B, 38 (12). F50-F60. ISSN 0740-3224

Published by: Optical Society of America

URL: <https://doi.org/10.1364/JOSAB.435068> <<https://doi.org/10.1364/JOSAB.435068>>

This version was downloaded from Northumbria Research Link:
<https://nrl.northumbria.ac.uk/id/eprint/47521/>

Northumbria University has developed Northumbria Research Link (NRL) to enable users to access the University's research output. Copyright © and moral rights for items on NRL are retained by the individual author(s) and/or other copyright owners. Single copies of full items can be reproduced, displayed or performed, and given to third parties in any format or medium for personal research or study, educational, or not-for-profit purposes without prior permission or charge, provided the authors, title and full bibliographic details are given, as well as a hyperlink and/or URL to the original metadata page. The content must not be changed in any way. Full items must not be sold commercially in any format or medium without formal permission of the copyright holder. The full policy is available online: <http://nrl.northumbria.ac.uk/policies.html>

This document may differ from the final, published version of the research and has been made available online in accordance with publisher policies. To read and/or cite from the published version of the research, please visit the publisher's website (a subscription may be required.)

A Simple Structure Dual-Core Photonic Crystal Fiber Polarization Beam Splitter Covering O+E+S+C+L+U Band Based on Surface Plasmon Resonance Effect

YUWEI QU,¹ JINHUI YUAN,^{1,2,5} SHI QIU,¹ XIAN ZHOU,² BINBIN YAN,¹ QIANG WU,^{3,4,6} BIN LIU,⁴ KUIRU WANG,¹ XINZHU SANG,¹ KEPING LONG,² AND CHONGXIU YU¹

¹State Key Laboratory of Information Photonics and Optical Communications, Beijing University of Posts and Telecommunications, Beijing 100876, China

²Research Center for Convergence Networks and Ubiquitous Services, University of Science & Technology Beijing, Beijing 100083, China

³Department of Physics and Electrical Engineering, Northumbria University, Newcastle upon Tyne, NE1 8ST, United Kingdom

⁴Key Laboratory of Nondestructive Test (Ministry of Education), Nanchang Hangkong University, Nanchang 330063, China

⁵yuanjinhui81@bupt.edu.cn

⁶qiang.wu@northumbria.ac.uk

Abstract: In this paper, a simple structure dual-core photonic crystal fiber (SS-DC-PCF) polarization beam splitter (PBS) based on surface plasmon resonance (SPR) effect and symmetric dual-core coupling mode theory is proposed. For the proposed SS-DC-PCF-1 PBS, the coupling lengths (*CLs*) and coupling length ratio (*CLR*) are analyzed, and the variations of the normalized output powers with the propagation length are investigated for the chosen wavelengths 1.434, 1.451, and 1.469 μm . The extinction ratio in the cores A and B are compared at the three splitting lengths (*SLs*) 170, 173, and 176 μm . When the optimal *SL* is 176 μm , the splitting bandwidth (*SB*) is 255 nm (1.437 ~ 1.692 μm), and the insertion loss (*IL*) is less than 0.043 dB. The regulations of the *CLs* and *CLR* with the change of the structure parameters are analyzed. For the proposed SS-DC-PCF-2 PBS, the optimal *SL* is 232 μm , the *SB* is 201 nm (1.249 ~ 1.450 μm), and the *IL* is less than 0.042 dB. Finally, it is demonstrated that the total *SB* of the proposed SS-DC-PCF-1 PBS and SS-DC-PCF-2 PBS is 443 nm (1.249 ~ 1.692 μm), which can cover the O + E + S + C + L + U band, even if the gold film thickness changes by ± 1 nm. The proposed SS-DC-PCF PBS has excellent performances, such as ultra-short *SL*, ultra-wide *SB*, ultra-low *IL*, and good error-tolerance rate. It will have important applications in the all-fiber optical systems.

© 2021 Optical Society of America

1. Introduction

The optical element, which can separate two beams of orthogonal polarized light according to two specific propagation directions, is called as polarization beam splitter (PBS) [1]. The PBS plays important roles in the fluorescence anisotropy (FA) measurement, optical coherence tomography (OCT), mode-locked fiber laser, etc.[2-5]. In the last decade, with the development of the micro/nano fiber fabrication technology, the requirement of all fiber optical systems on the high performance fiber PBS has been continuously increased [6-9].

At present, the used fiber PBSs are mainly divided into three categories, which include traditional fiber PBS, microfiber PBS, and photonic crystal fiber (PCF) PBS [10-15]. For the traditional fiber PBS, it is difficult to achieve the good performance and miniaturization due to the single fiber structure and material. Although the microfiber PBS can achieve good

beam splitting characteristic and have short length, it is difficult to implement the device packaging in practical application because of the small microfiber diameter. Because the PCF contains many micron scale air holes in the cladding region, the cladding structure can be designed flexibly according to the actual requirements. For example, some functional materials can be selectively filled or coated in or on the air holes to achieve the PBS. Moreover, compared with the microfiber, the diameter of the PCF is much larger, which is conducive to the device packaging. Therefore, the PCF PBS has become the research hotspot.

In recent years, the researchers have studied the dual-core (DC) and three-core PCF PBS, but the three-core PCF is more difficult to fabricate than that of the DC-PCF [16-20]. Therefore, some investigations are mainly focused on the DC-PCF PBS. In 2019, Zhao et al. designed a hexagonal lattice DC-PCF PBS with two elliptical air holes and two gold-coated air holes based on the surface plasmon resonance (SPR) effect, whose splitting length (SL) is 104 μm and splitter bandwidth (SB) covers the S + C + L + U band [21]. In 2020, Chen et al. reported a short PBS based on the DC-PCF with As_2S_3 layer, whose SL is 1.0 mm, SB is 280 nm, and insertion loss (IL) of X-polarized light is as low as 0.18 dB [22]. In 2021, Nelson et al. proposed a thermo optically tunable PBS based on the two gold wires filled DC-PC with integrated electrodes, whose SL and SB are 1.890 mm and 9 nm, respectively [23]. However, the above proposed DC-PCF PBS structures are very complex, which greatly increases the difficulty of fabrication. In addition, the SB of the proposed DC-PCF PBS does not cover all commonly used communication bands. To meet the practical requirements, it is necessary to design the DC-PCF PBS with simple structure and good performances. In this paper, we propose a simple structure DC-PCF (SS-DC-PCF) PBS based on the SPR effect and symmetric dual-core coupling mode theory. The coupling lengths (CLs) and coupling length ratio (CLR) of the SS-DC-PCF-1 PBS are analyzed. The influences of the structure parameters on the CLs and CLR are investigated. The variations of the normalized output power (P_{out}) with the propagation length (PL) of the SS-DC-PCF-1 PBS and SS-DC-PCF-2 PBS are investigated. The extinction ratios (ERs) in the cores A and B, the maximum ILs , and the error-tolerance rate (ETR) of the SS-DC-PCF-1 PBS and SS-DC-PCF-2 PBS are also demonstrated, respectively. Finally, the total SB of the SS-DC-PCF-1 PBS and SS-DC-PCF-2 PBS covers the O + E + S + C + L + U band.

2. Design of the SS-DC-PCF PBS

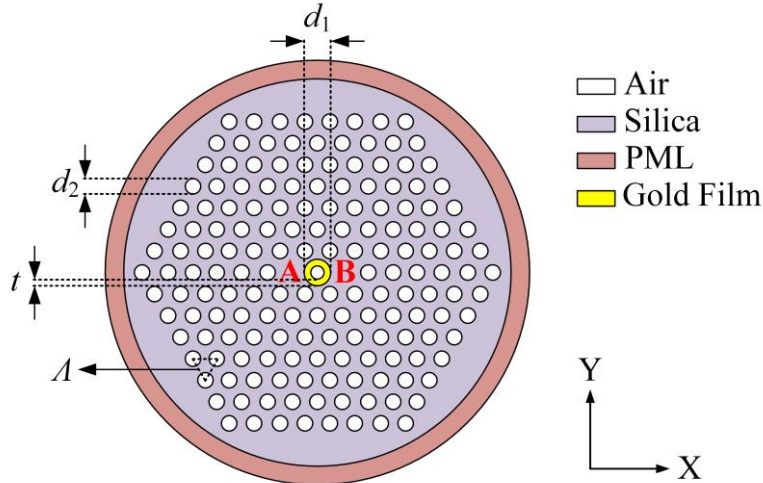


Fig. 1. The cross-sectional structure of the proposed SS-DC-PCF PBS.

The cross-sectional structure of the proposed SS-DC-PCF PBS is shown in Fig. 1. From Fig. 1, the proposed SS-DC-PCF has eight layers of air holes, which are arranged in the triangular

lattice. In order to reduce the structural complexity and fabrication cost, a thin gold film with the thickness of t is selectively coated on the central air hole, whose diameter is d_1 . Compared with other metal materials, the gold material has stable chemical properties and strong corrosion resistance [24]. When the incident light energy is propagated inside the SS-DC-PCF coated with the gold film on the central air hole, the free electrons on the gold film surface of the most central air hole interact with the incident light energy to produce the SPR effect and excite the surface plasmon polariton (SPP) mode on the gold film surface [25]. The core mode and SPP mode of the SS-DC-PCF will have the same propagation constant at some specific wavelengths. Therefore, the mode coupling will occur between the core mode and SPP mode due to the satisfaction of the phase matching conditions. Two air holes are missing on the left and right sides of the central air hole, forming the cores A and B, respectively. The diameter of other air holes is d_2 , the hole to hole pitch is A , and the substrate material is the silica. The finite element method (FEM) is used to carry out the calculation [26]. In order to absorb the radiation energy, a perfect matching layer (PML) with the thickness of d_2 is added to the outermost layer of the proposed SS-DC-PCF, and the refractive index of the PML (n_{PML}) is 0.03 higher than that of the silica material [27]. In addition, the cross-sectional structure of the proposed SS-DC-PCF is meshed before the calculation. In the calculation, the mesh sizes of the silica and air holes are set as $\lambda/6$, the mesh sizes of the cores A and B are set as $\lambda/4$, the mesh size of PML is set as $\lambda/2$, and the mesh size of the central air hole coated with the gold film is set as $\lambda/60$. The complete grid consists of 8792 domain elements and 994 boundary elements.

The refractive index of the silica material (n_{silica}) can be obtained by the Sellmeier equation [28]

$$n_{\text{silica}}(\lambda) = \sqrt{1 + \frac{A_1 \lambda^2}{\lambda^2 - B_1^2} + \frac{A_2 \lambda^2}{\lambda^2 - B_2^2} + \frac{A_3 \lambda^2}{\lambda^2 - B_3^2}}, \quad (1)$$

where λ is the wavelength of the initial incident light. The detailed parameters in Eq. (1) for n_{silica} are given in Table 1.

The relative dielectric constant of the gold material (ϵ_m) can be calculated by the Drude-Lorentz model [29]

$$\epsilon_m = \epsilon_\infty - \frac{\omega_D^2}{\omega(\omega - j\gamma_D)} - \frac{\Delta\epsilon \cdot \Omega_L^2}{(\omega^2 - \Omega_L^2) - j\Gamma_L \omega}, \quad (2)$$

where ω is the angle frequency of the guided-wave, ϵ_∞ is the high frequency dielectric constant, $\Delta\epsilon$ is the weighted coefficient, ω_D and γ_D are the plasma and damping frequencies, and Ω_L and Γ_L are the frequency and bandwidth of the Lorentz oscillator, respectively. The detailed parameters in the Eq. (2) for ϵ_m are also given in Table 1.

Table 1. The detailed parameters in Eq. (1) for n_{silica} and Eq. (2) for ϵ_m .

	A_1	A_2	A_3	B_1 (μm)	B_2 (μm)	B_3 (μm)
Silica	0.6961663	0.4079426	0.8974794	0.0684043	0.1162414	9.896161
	ϵ_∞	$\Delta\epsilon$	$\omega_D/2\pi$ (THz)	$\gamma_D/2\pi$ (THz)	$\Omega_L/2\pi$ (THz)	$\Gamma_L/2\pi$ (THz)
Gold	5.9673	1.09	2113.6	15.92	650.07	104.86

The CLs of the X-polarization (X-pol) and Y-polarization (Y-pol) of the SS-DC-PCF PBS can be expressed as [30]

$$CL_X = \frac{\lambda}{2|(n_{\text{even}}^X - n_{\text{odd}}^X)|}, \quad (3)$$

$$CL_Y = \frac{\lambda}{2|(n_{\text{even}}^Y - n_{\text{odd}}^Y)|}, \quad (4)$$

where CL_X and CL_Y stand for the CL of the X-pol and Y-pol, respectively, λ is the wavelength of the initial incident light, and n_X even, n_X odd, n_Y even and n_Y odd stand for the real parts of the effective refractive indices $\text{Re}(n_{\text{eff}})$ of the even and odd modes of the X-pol and Y-pol, respectively.

The CLR can be obtained by [31]

$$CLR = \frac{CL_Y}{CL_X}, \quad (5)$$

When the $CLR=2$ or $1/2$, the SL will have an optimal length, which can be considered as the shortest length of the PBS.

P_{out} of the X-pol and Y-pol in the cores A and B can be calculated by [32]

$$P_{\text{out,A}}^{X,Y} = P_{\text{in}} \cos^2\left(\frac{\pi}{2} \frac{PL}{CL_{X,Y}}\right), \quad (6)$$

$$P_{\text{out,B}}^{X,Y} = P_{\text{in}} \sin^2\left(\frac{\pi}{2} \frac{PL}{CL_{X,Y}}\right), \quad (7)$$

where P_{in} is the power of the initial incident light, and PL is the propagation length inside the SS-DC-PCF PBS. In general, the PL is equal to the shortest SL .

The ER s of the cores A and B, which are considered as an important parameter to evaluate the splitting performance of the SS-DC-PCF PBS, can be described as [33]

$$ER_A = 10 \log_{10} \frac{P_{\text{out,A}}^X}{P_{\text{out,A}}^Y}, \quad (8)$$

$$ER_B = 10 \log_{10} \frac{P_{\text{out,B}}^Y}{P_{\text{out,B}}^X}, \quad (9)$$

The higher the ER , the better the splitting performance of the PBS. Usually, the wavelength range corresponding to the ER greater than 20 dB is considered as the SB of the PBS.

The IL s of the X-pol and Y-pol of the SS-DC-PCF PBS are also significant parameters, which can be calculated by [34]

$$IL_X = -10 \log_{10} \frac{P_{\text{out}}^X}{P_{\text{in}}}, \quad (10)$$

$$IL_Y = -10 \log_{10} \frac{P_{\text{out}}^Y}{P_{\text{in}}}, \quad (11)$$

3. Simulation results and discussion

For the proposed SS-DC-PCF PBS, the cores A and B have the same structure and are completely symmetrical. Therefore, the initial incident light propagated in any one of the cores will have the same result. Here, we assume that the initial incident light propagated in the core A, and the calculations are carried out by the FEM. In the simulation, two sets of structural parameters are chosen, and the corresponding PBSs are called as SS-DC-PCF-1 PBS and SS-DC-PCF-2 PBS, respectively. The parameters of the proposed SS-DC-PCF-1 are set as following: $d_1=1.10 \mu\text{m}$, $d_2=1.30 \mu\text{m}$, $\Lambda=2.12 \mu\text{m}$, and $t=50 \text{ nm}$. The variations of $\text{Re}(n_{\text{eff}})$

of the X-pol and Y-pol even and odd modes and second-order SPP mode (2nd-order SPP mode) with wavelength are shown in Figs. 2 (a) and 2(b), respectively. From Figs. 2 (a) and 2(b), $\text{Re}(n_{\text{eff}})$ of the X-pol and Y-pol even modes monotonously decreases with the increase of wavelength in the range of 1.1 ~ 1.8 μm . In contrast, $\text{Re}(n_{\text{eff}})$ of the X-pol and Y-pol odd modes first decreases with the increase of wavelength in the ranges of 1.1 ~ 1.328 μm and 1.1 ~ 1.285 μm , and then increases suddenly at wavelengths 1.328 and 1.285 μm . Finally, $\text{Re}(n_{\text{eff}})$ of the X-pol and Y-pol odd modes continues to decrease as the wavelength increases in the ranges of 1.328 ~ 1.8 μm and 1.285 ~ 1.8 μm , respectively. Meanwhile, $\text{Re}(n_{\text{eff}})$ of the 2nd-order SPP mode decreases suddenly at wavelengths 1.328 and 1.285 μm , respectively. That is, $\text{Re}(n_{\text{eff}})$ of the X-pol and Y-pol odd modes has the cross points with $\text{Re}(n_{\text{eff}})$ of the 2nd-order SPP mode at wavelengths 1.328 and 1.285 μm , respectively. According to the symmetric dual-core coupling mode theory [35], the two cross points of $\text{Re}(n_{\text{eff}})$ are called as the X-pol and Y-pol phase-matching wavelengths (λ_p), respectively. And the X-pol and Y-pol odd modes occur to couple with the 2nd-order SPP mode at the X-pol λ_p 1.328 μm and the Y-pol λ_p 1.285 μm , respectively. But there is no coupling between the X-pol and Y-pol even modes and 2nd-order SPP mode at any wavelength in the range of 1.1 ~ 1.8 μm . The six insets in Figs. 2(a) and 2(b) show the mode field distributions of the X-pol and Y-pol even and odd modes and 2nd-order SPP mode of the SS-DC-PCF-1 at wavelengths 1.328 and 1.285 μm , respectively. From the insets in Figs. 2 (a) and 2(b), there is no change in the mode field energy of the X-pol and Y-pol even modes at wavelengths 1.328 and 1.285 μm , respectively. However, the mode field energy of the X-pol and Y-pol odd modes and 2nd-order SPP mode occurs to exchange at wavelengths 1.328 and 1.285 μm , respectively. It is clearly confirmed from the insets that only the X-pol and Y-pol odd modes occur to couple with the 2nd-order SPP mode at wavelengths 1.328 and 1.285 μm , respectively.

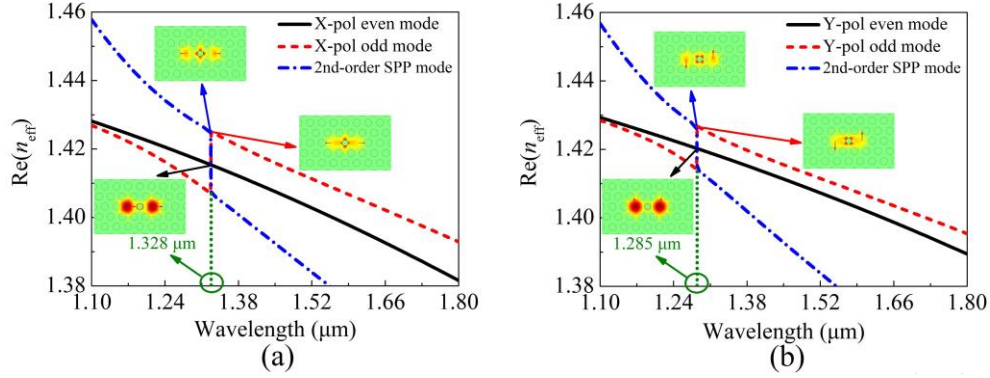


Fig. 2. The variations of $\text{Re}(n_{\text{eff}})$ of the (a) X-pol and (b) Y-pol even and odd modes and second-order SPP mode with wavelength. The six insets show the mode field distributions of the X-pol and Y-pol even and odd modes and 2nd-order SPP mode of the SS-DC-PCF-1 at wavelengths 1.328 and 1.285 μm , respectively.

Fig. 3 shows the variations of the CL_X , CL_Y , and CLR of the proposed SS-DC-PCF-1 in the wavelength range of 1.1 ~ 1.8 μm . It can be seen from Fig. 3 that the CL_X and CL_Y decrease rapidly before the wavelengths 1.328 and 1.285 μm . Then, the CL_X and CL_Y have the distinct turning points at wavelengths 1.328 and 1.285 μm , which correspond to the X-pol and Y-pol λ_p s, respectively. After the two distinct turning points, the CL_X and CL_Y first increase slowly and then decrease gradually, respectively. Because the X-pol and Y-pol have different λ_p s, according to the calculation result of Eq. (5), the CLR decreases rapidly before wavelength 1.285 μm . Then, the CLR has a significant change in the wavelength range from 1.285 to 1.328 μm . After wavelength 1.328 μm , the CLR first increases slowly and then decreases gradually. On the whole, the CLR increases or decreases near $CLR = 2$. The CLR is exactly equal to 2 at wavelengths 1.434 and 1.609 μm , respectively. The maximum value of

the CLR between wavelengths 1.434 and 1.609 μm is only 2.018, so the value of the CLR can be approximately equal to 2. According to the previous work [36], when the working wavelength is located between wavelengths 1.434 and 1.609 μm where $CLR = 2$, it may be beneficial to obtain a wider SB . Moreover, the CL_X and CL_Y increase first and then decrease between wavelengths 1.434 and 1.609 μm , so the CL_X and CL_Y will have two approximately equal values near wavelengths 1.434 and 1.609 μm , respectively. Therefore, we only need to consider the case that the corresponding wavelength position of the CL_X and CL_Y is closer to wavelength 1.434 or 1.609 μm . In this work, we only demonstrate the results near wavelength 1.434 μm .

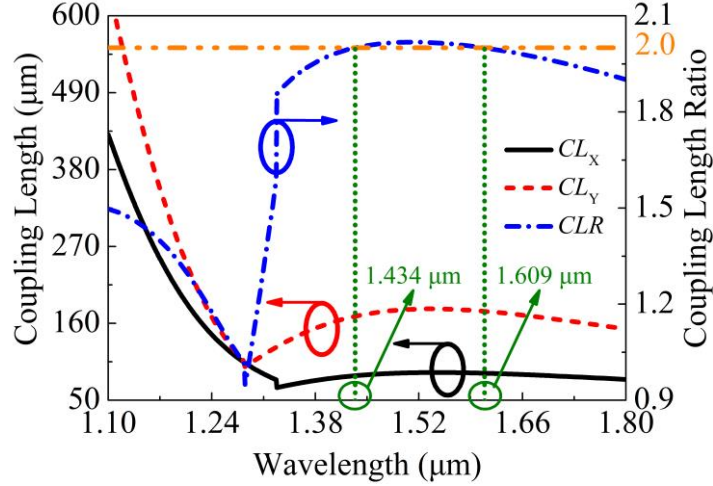


Fig. 3. The CL_X , CL_Y , and CLR of the proposed SS-DC-PCF-1 as functions of the wavelength.

From Fig. 3, the CL_X and CL_Y are approximately equal to 85, 86.5, and 88 μm , and 170, 173, and 176 μm at the three wavelengths 1.434, 1.451, and 1.469 μm , respectively. The relationships between P_{out} of the X-pol and Y-pol in the cores A and B of the proposed SS-DC-PCF-1 PBS and PL at the three wavelengths 1.434, 1.451, and 1.469 μm are shown in Figs. 4(a - b), 4(c - d), and 4(e - f), respectively. As seen from Fig. 4, P_{out} of the X-pol and Y-pol in the cores A and B changes periodically with the increase of PL . From Figs. 4(a), 4(c), and 4(e), P_{out} of the X-pol in the core A reaches the maximum value for the first time at the PL s of 170, 173, and 176 μm , respectively. At the same time, P_{out} of the Y-pol in the core A reaches 0 for the first time at the PL s of 170, 173, and 176 μm , respectively. It can be concluded that only the X-pol light exists in the core A when the PL s are 170, 173, and 176 μm , respectively. On the contrary, from Figs. 4(b), 4(d), and 4(f), P_{out} of the X-pol in the core B reaches 0 for the first time at the PL s of 170, 173 and 176 μm , respectively. Meanwhile, P_{out} of the Y-pol in the core B reaches the maximum value for the first time at the PL s of 170, 173, and 176 μm , respectively. It can be concluded that only the Y-pol light exists in the core B when the PL s are 170, 173, and 176 μm , respectively. Based on the above results, the SL of the proposed SS-DC-PCF-1 PBS may be 170, 173, or 176 μm . In addition, we also observe an interesting phenomenon from Fig. 4 that the total P_{out} decreases slightly with the increase of PL . The main reason is considered that when the light is propagated in the proposed SS-DC-PCF-1 PBS, the energy propagated on the gold film surface is very little, and will be lost in the form of ohmic loss.

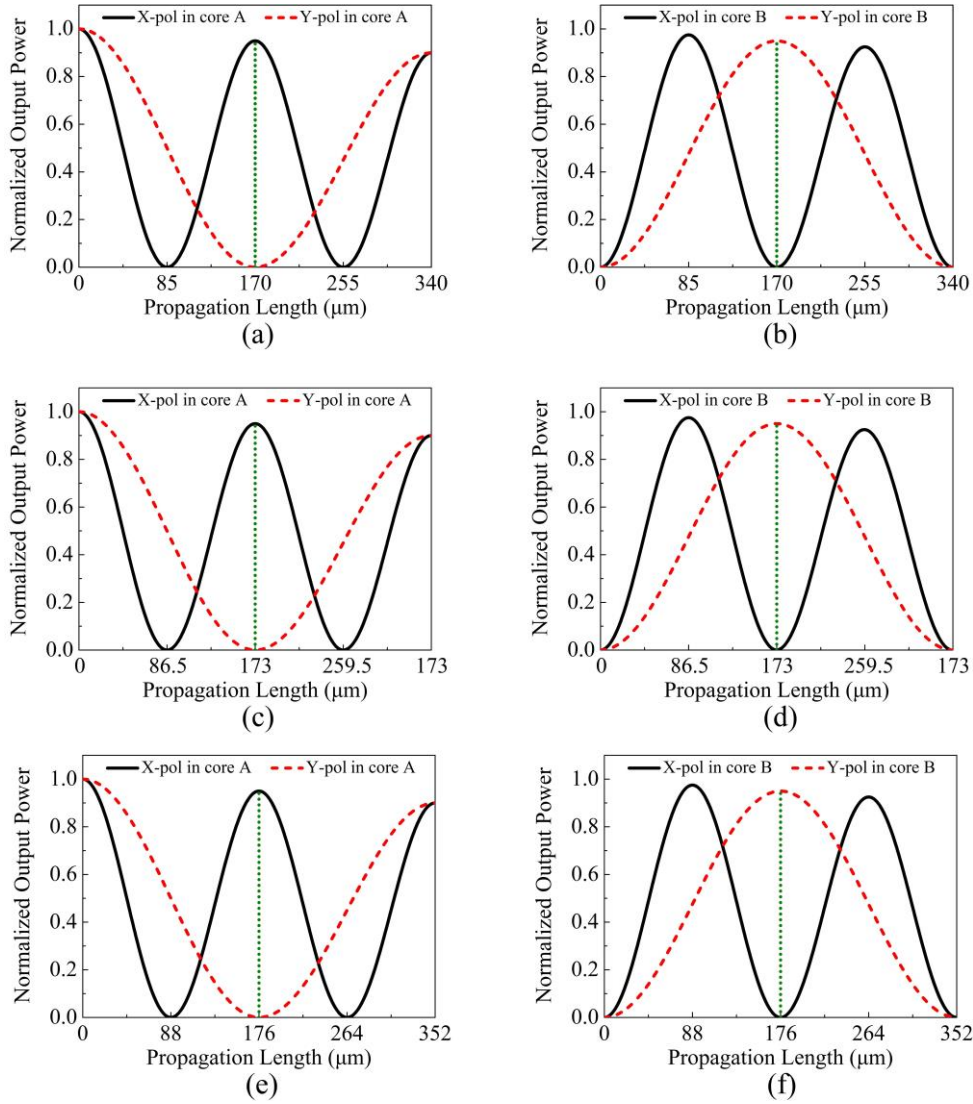


Fig. 4. The relationships between the normalized output powers P_{out} of the X-pol and Y-pol of the proposed SS-DC-PCF-1 PBS and PL at (a - b) 1.434, (c - d) 1.451, and (e - f) 1.469 μm , respectively.

Figs. 5(a) and 5(b) show the relationships between the ER s in the cores A and B of the proposed SS-DC-PCF-1 PBS and wavelength when the SL is 170, 173, and 176 μm , respectively. From Fig. 5(a), the ER in the core A is always greater than 20 dB in a wide wavelength range when the SL is equal to 170, 173, or 176 μm . From Fig. 5(b), only when the SL is equal to 176 μm , the ER in the core B can be greater than 20 dB in the considered wavelength range. When the SL is equal to 170 or 173 μm , the ER in the core B is always less than 20 dB in a certain wavelength range. The wavelength range with ER greater than 20 dB can be defined as the SB of the PBS. Thus, in order to analyze the SB s in the cores A and B of the proposed SS-DC-PCF-1 PBS more intuitively, the SB s in the cores A and B of the proposed SS-DC-PCF-1 PBS at $SL=170, 173,$ and $176 \mu\text{m}$ are shown in Table 2. From Table 2, the SB in the core A covers a complete and wide wavelength range. The narrowest SB in the core A is 1.417 ~ 1.707 μm when the SL is equal to 176 μm . But only when SL is equal to 176 μm , the SB in the core B covers a complete and wide wavelength range (1.437 ~ 1.692

μm). When the SL is equal to 170 or 173 μm , the SB in the core B is divided into the two wave bands. Therefore, in order to ensure the SB s in the cores A and B can cover a complete and wide wavelength range, the optimal length SL of the proposed SS-DC-PCF-1 PBS is chosen as 176 μm . However, when the SL is 176 μm , the SB in the core A is inconsistent with that in the core B. Considering the two SB s synthetically, the final SB of the proposed SS-DC-PCF-1 PBS is 255 nm (1.437 ~ 1.692 μm). The relationships between the IL s in the X-pol and Y-pol of the proposed SS-DC-PCF-1 PBS and wavelength are shown in Fig. 6 when the SL is 176 μm . From Fig. 6, both the X-pol and Y-pol have very small IL in the whole SB . The maximum IL of the X-pol is only 0.043 dB at wavelength 1.437 μm , while that of the Y-pol is only 0.027 dB at wavelength 1.692 μm .

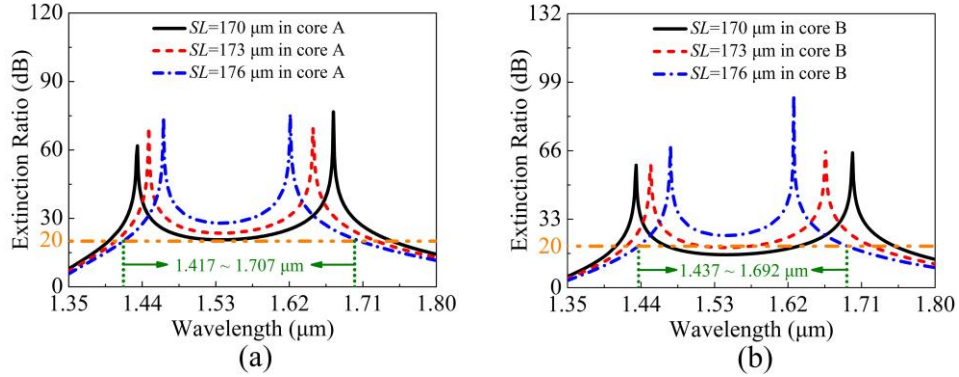


Fig. 5. The ER s in the cores (a) A and (b) B of the proposed SS-DC-PCF-1 PBS as functions of the wavelength when the SL is 170, 173, and 176 μm , respectively.

Table 2. The SB s in the cores A and B of the proposed SS-DC-PCF-1 PBS at $SL=170, 173,$ and $176 \mu\text{m}$, respectively.

SL (μm)	SB in the core A (μm)	SB in the core B (μm)
170	1.399 ~ 1.746	1.410 ~ 1.471 and 1.633 ~ 1.750
173	1.410 ~ 1.726	1.423 ~ 1.516 and 1.575 ~ 1.722
176	1.417 ~ 1.707	1.437 ~ 1.692

According to the above results, the SB of the proposed SS-DC-PCF-1 PBS is 255 nm (1.437 ~ 1.692 μm), which only covers the optical communication S + C + L + U band. However, if only one SS-DC-PCF-1 PBS is proposed, the final SB could not cover the commonly used O + E + S + C + L + U band (1.260 ~ 1.675 μm). If another SS-DC-PCF-2 PBS with different SB can be proposed by adjusting the fiber structure parameters and the total SB of the SS-DC-PCF-1 PBS and SS-DC-PCF-2 PBS can cover the whole optical communication band, it will be much more meaningful. Therefore, it is necessary to analyze the influences of the structure parameters d_1 , d_2 , A , and t of the proposed SS-DC-PCF-1 on the CL s and CLR , respectively.

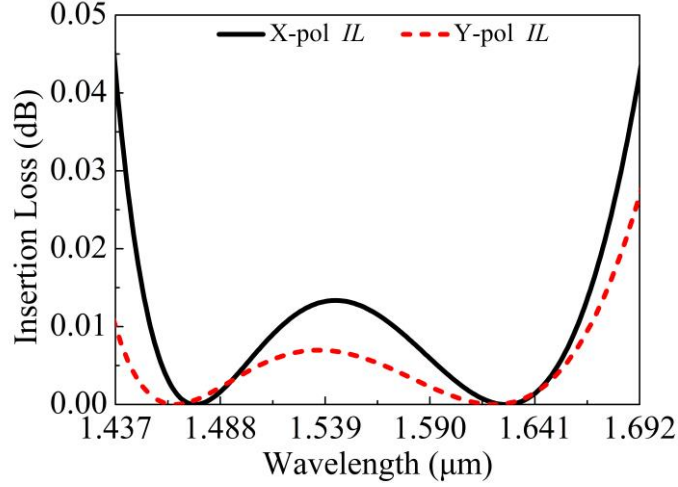


Fig. 6. The ILs of the X-pol and Y-pol of the proposed SS-DC-PCF-1 PBS as functions of the wavelength.

First, the variations of the CL_X , CL_Y , and CLR of the proposed SS-DC-PCF-1 as functions of the wavelength are shown in Figs. 7(a) and 7(b) when d_1 is set to 1.00, 1.10, and 1.20 μm , respectively. From Fig. 7(a), the value of the CL_X decreases with the increase of d_1 in the whole wavelength range, and the decrease amplitude at the short wavelength is greater than that at the long wavelength. Meanwhile, the X-pol λ_p shifts to the long wavelength direction with the increases of d_1 . It can also be observed from Fig. 7(a) that the variation of the Y-pol λ_p and the value of the CL_Y at the short wavelength with d_1 is the same as that of the X-pol λ_p and the value of the CL_Y at the short wavelength, respectively. The only difference is that with the increase of d_1 , the value of the CL_Y at the long wavelength will not change basically. According to the change of the CL_X and CL_Y with d_1 , the change of the CLR with d_1 can be deduced, as shown in Fig. 7(b). From Fig. 7(b), it is obvious that the value of the CLR increases and the X-pol and Y-pol λ_p s shift to the long wavelength direction with the increases of d_1 . Therefore, the change of d_1 can adjust the X-pol and Y-pol λ_p s and the value of CLR .

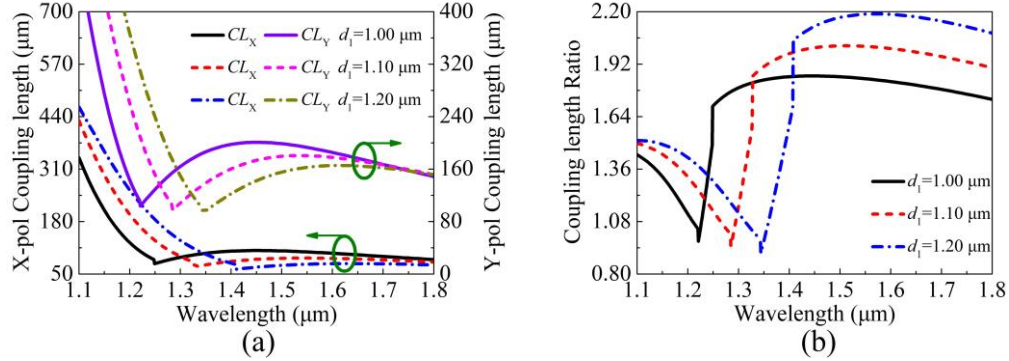


Fig. 7. The variations of the (a) CL_X , CL_Y , and (b) CLR of the proposed SS-DC-PCF-1 PBS for different d_1 .

Second, the variations of the CL_X , CL_Y , and CLR of the proposed SS-DC-PCF-1 as functions of the wavelength are shown in Figs. 8(a) and 8(b) when d_2 is set to 1.20, 1.30, and 1.40 μm , respectively. It can be seen from Fig. 8(a) that the value of the CL_X decreases uniformly with the increases of d_2 in the whole wavelength range, but the decrease amplitude is very small. At the same time, the X-pol λ_p shifts to the long wavelength direction with the

increase of d_2 , but the shift range is also very small. In contrast, the value of the CL_Y and the Y-pol λ_p do not change with the increase of d_2 in the whole wavelength range. As seen from Fig. 8(b), with the increases of d_2 , the value of the CLR increases and the Y-pol λ_p basically does not change, while the X-pol λ_p is slightly shifted to the long wavelength direction. Therefore, the change of d_2 can only adjust the value of CLR .

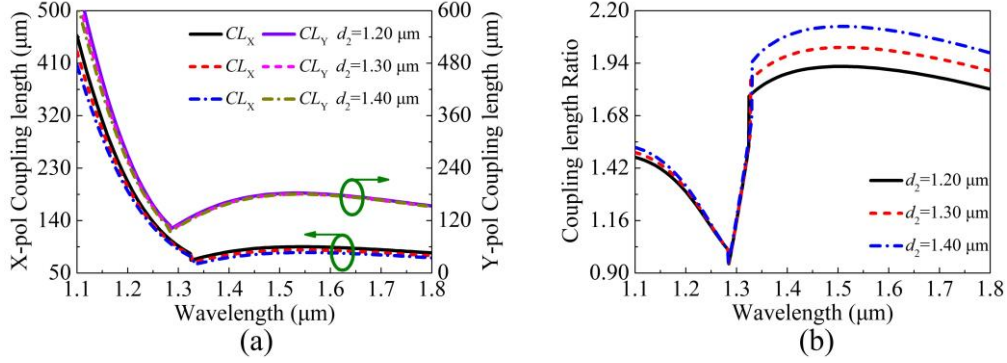


Fig. 8. The variations of the (a) CL_X , CL_Y , and (b) CLR of the proposed SS-DC-PCF-1 PBS for different d_2 .

Third, the variations of the CL_X , CL_Y , and CLR of the proposed SS-DC-PCF-1 as functions of the wavelength are shown in Figs. 9(a) and 9(b) when A is set to 2.02, 2.12, and 2.22 μm, respectively. From Fig. 9(a), the value of the CL_X and CL_Y increases uniformly with the increases of A in the whole wavelength range, and the X-pol and Y-pol λ_{ps} have a small shift range to the short wavelength direction. It can be seen from Fig. 9(b) that the value of the CLR decreases with the increases of A , and the X-pol and Y-pol λ_{ps} shift a small range to the short wavelength direction. Therefore, the change of A can not only adjust the value of the CLR , but also adjust the X-pol and Y-pol λ_{ps} .

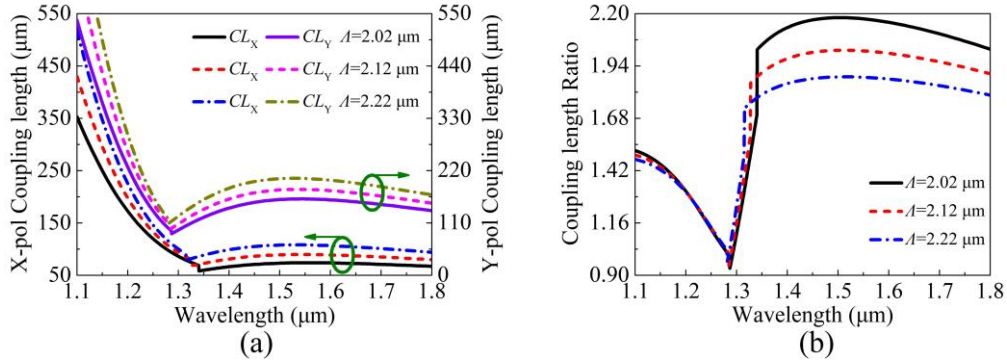


Fig. 9. The variations of the (a) CL_X , CL_Y , and (b) CLR of the proposed SS-DC-PCF-1 PBS for different A .

Finally, the variations of the CL_X , CL_Y and CLR of the proposed SS-DC-PCF-1 as functions of the wavelength are shown in Figs. 10(a) and 10(b) when t is set to 45, 50, and 55 nm, respectively. From Fig. 10(a), the value of the CL_X increases with the increase of t at the short wavelength, but the increase amplitude is very small. But the value of the CL_X does not change with the increase of t at the long wavelength. In addition, it is also found that the X-pol λ_{ps} shifts to the short wavelength direction. Although the Y-pol λ_{ps} has the same change trend, the value of the CL_Y increases at the short wavelength and decreases slightly at the long wavelength. It can be seen from Fig. 10(b) that with the increases of t , the value of the CLR remains near $CLR = 2.0$ and the X-pol and Y-pol λ_{ps} are also shifted to the short

wavelength direction. On the whole, compared with the other three parameters, the change of t can only adjust the X-pol and Y-pol λ_{ps} .

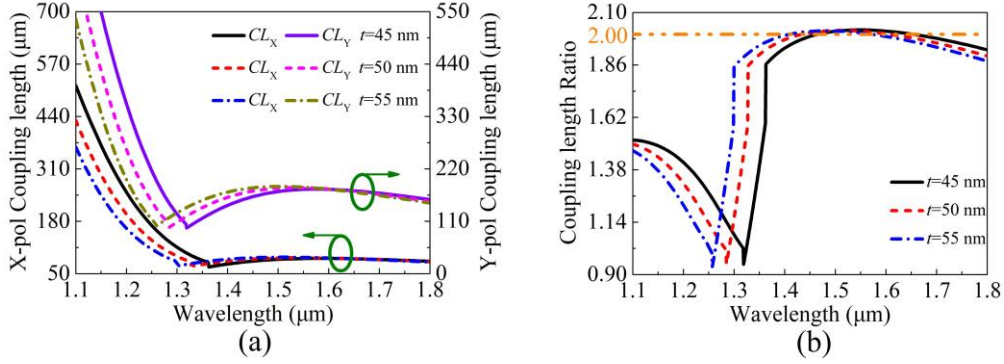


Fig. 10. The variations of the (a) CL_X , CL_Y , and (b) CLR of the proposed SS-DC-PCF-1 PBS for different t .

According to the above investigations, the SS-DC-PCF-2 PBS can be designed. Therefore, it is necessary to make the X-pol and Y-pol λ_{ps} located before wavelength 1.260 μm and keep the CLR near 2.0 by adjusting d_1 , d_2 , A , and t . The structure parameters of the proposed SS-DC-PCF-2 are set as $d_1=0.90$ μm, $d_2=1.72$ μm, $A=2.14$ μm, and $t=60$ nm. Fig. 11 shows the variations of the CL_X , CL_Y , and CLR of the proposed SS-DC-PCF-2 with wavelength in the range of 1.1 ~ 1.8 μm. From Fig. 11, the X-pol and Y-pol λ_{ps} are 1.139 and 1.115 μm, respectively. Similar to the previous analysis of the proposed SS-DC-PCF-1, the CLR of the proposed SS-DC-PCF-2 also first increases slowly and then decreases gradually after wavelength 1.139 μm. However, on the whole, the CLR increases or decreases near $CLR=2$. The CLR is exactly equal to 2 at wavelengths 1.232 and 1.434 μm, respectively, and the maximum value of the CLR between 1.232 and 1.434 μm is only 2.023, so the value of the CLR between 1.232 and 1.434 μm can be approximately equal to 2. Similarly, near wavelengths 1.232 and 1.434 μm, the CL_X and CL_Y will have two approximately equal values, respectively. Here, we only consider the results of the CL_X and CL_Y near wavelength 1.434 μm. In addition, From Fig. 11, the CL_X and CL_Y are approximately equal to 116, 115, and 114 μm, and 232, 230, and 228 μm at the three wavelengths 1.411, 1.422 and 1.434 μm, respectively. Based on the previous analysis of the proposed SS-DC-PCF-1 and the theoretical calculation, the CL_X and CL_Y at wavelength 1.411 μm are finally selected for the further analysis. The relationships between P_{out} of the X and Y-pol in the cores A and B of the proposed SS-DC-PCF-2 PBS and PL at wavelength 1.411 μm are shown in Figs. 12(a) and 12(b), respectively. From Figs. 12(a) and 12(b), P_{out} of the X-pol and Y-pol in the cores A and B reach the maximum value for the first time when the PL is 232 μm, respectively. Meanwhile, P_{out} of the X-pol and Y-pol in the cores A and B reach 0 for the first time when the PL is 232 μm, respectively. Therefore, it can be inferred that there is only the X-pol light in the core A and Y-pol light in the core B. Due to the existence of the ohmic loss on the gold film surface, the interesting phenomenon that the total P_{out} decreases slightly with the increase of the PL still exists.

Figs. 13(a) and 13(b) show the relationships between the ERs in the cores A and B of the proposed SS-DC-PCF-2 PBS and wavelength when the SL is 232 μm, respectively. It can be seen from Figs. 13(a) and 13(b) that the ERs in the cores A and B are always greater than 20 dB in a wide wavelength range when the SL is 232 μm. Therefore, the SL of the proposed SS-DC-PCF-2 PBS is 232 μm, and the SBs in the cores A and B of the proposed SS-DC-PCF-2 PBS are 244 nm (1.232 ~ 1.476 μm) and 201 nm (1.249 ~ 1.450 μm), respectively. Considering the two SBs synthetically, the final SB of the proposed SS-DC-PCF-1 PBS is 201 nm (1.249 ~ 1.450 μm). The relationships between the ILs in the

X-pol and Y-pol of the proposed SS-DC-PCF-2 PBS and wavelength when the SL is $232 \mu\text{m}$ are shown in Fig. 14. From Fig. 14, the maximum IL of the X-pol is only 0.042 dB at wavelength $1.249 \mu\text{m}$, while that of the Y-pol is only 0.012 dB at wavelength $1.450 \mu\text{m}$.

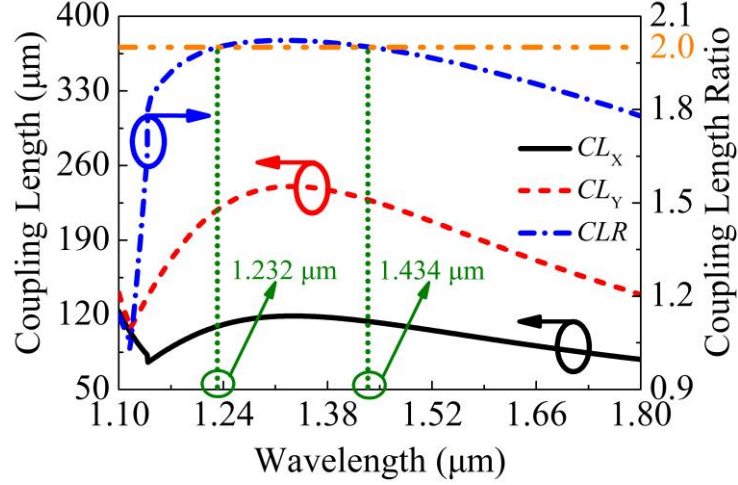


Fig. 11. The CL_x , CL_y , and CLR of the proposed SS-DC-PCF-2 as functions of the wavelength.

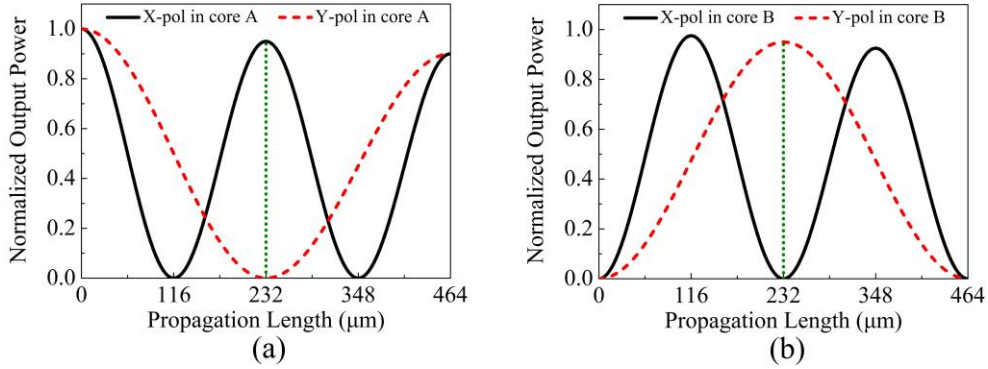


Fig. 12. The relationships between the output powers P_{out} of the X and Y-pol of the proposed SS-DC-PCF-2 PBS and PL in the cores (a) A and (b) B at wavelength $1.411 \mu\text{m}$, respectively.

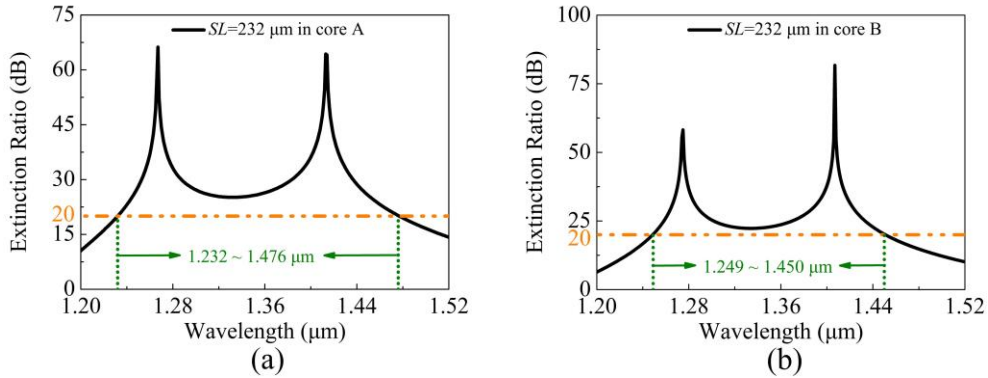


Fig. 13. The ERs in the cores (a) A and (b) B of the proposed SS-DC-PCF-2 PBS as functions of the wavelength when the SL is $232 \mu\text{m}$, respectively.

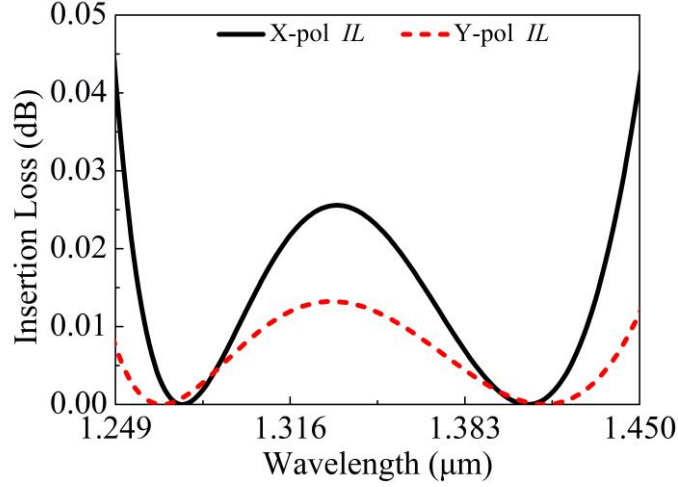


Fig. 14. The *ILs* of the X-pol and Y-pol of the proposed SS-DC-PCF-2 PBS as functions of the wavelength.

To sum up, the total *SB* of the proposed SS-DC-PCF-1 PBS and SS-DC-PCF-2 PBS is 443 nm (1.249 ~ 1.692 μm), which can cover the O + E + S + C + L + U band (1.260 ~ 1.675 μm). In the following, it is necessary to consider the problems existing in the actual fabrication of the proposed SS-DC-PCF. The fabrication methods mainly include the stack-and-draw method, femtosecond laser drilling method, 3D printing method, etc. [37-40]. In addition, the technology of selectively coating the metal film on the air holes has also been very mature, including chemical vapor deposition, radio frequency magnetron sputtering, etc. [41-44]. In this work, the fabrication of the proposed SS-DC-PCF is mainly divided into the two steps. First, the proposed SS-DC-PCF is fabricated by the stack-and-draw method. With this method, the high-purity silica glass tubes are arranged according to the designed structure, two high-purity silica solid rods are used to replace the high-purity silica glass tubes on the left and right sides of the most central high-purity silica glass tubes, respectively, to form SS-DC-PCF preform, and the SS-DC-PCF preform is drawn into the designed SS-DC-PCF. Second, the gold film is deposited in the central air hole of the SS-DC-PCF by high pressure chemical vapor deposition. However, for selective gold film coating technology, it is difficult to achieve the complete stability, so it is necessary to consider the *ETR* caused by the uneven *t* in the fabrication process.

Here, we set the error range of the selective *t* in the fabrication process to ± 1 nm. That is to say, the error ranges of *t* of the proposed SS-DC-PCF-1 PBS and SS-DC-PCF-2 PBS are 49, 50, and 51 μm , and 59, 60, and 61 μm , respectively. Figs.15 (a ~ b) and (c ~ d) show the *ERs* in the cores A and B of the proposed SS-DC-PCF-1 PBS and SS-DC-PCF-2 PBS as functions of the wavelength when *t* is 49, 50, and 51 μm , and 59, 60, and 61 μm , respectively. From Figs.15 (a ~ d), the *ERs* in the cores A and B of the proposed SS-DC-PCF-1 PBS and SS-DC-PCF-2 PBS are always greater than 20 dB in a wide wavelength range. In order to observe more clearly the change of the *SBs* in the cores A and B of the proposed SS-DC-PCF-1 PBS and SS-DC-PCF-2 PBS, the *SBs* in the cores A and B of the proposed SS-DC-PCF-1 PBS (*SL* = 176 μm) and SS-DC-PCF-2 PBS (*SL* = 232 μm) are shown in Table 3 when *t* is 49, 50, and 51 μm , and 59, 60, and 61 μm , respectively. It can be seen from Table 3 that the *SBs* in the cores A and B of the proposed SS-DC-PCF-1 PBS and SS-DC-PCF-2 PBS change little when *t* changes. The narrowest *SBs* of the proposed SS-DC-PCF-1 PBS and SS-DC-PCF-2 PBS are 247 nm (1.447 ~ 1.694 μm) and 196 nm (1.255 ~ 1.451 μm) when *t* is 49 and 59 nm, respectively. Therefore, the narrowest total *SB* of the proposed SS-DC-PCF-1 PBS and SS-DC-PCF-2 PBS is 439 nm (1.255 ~ 1.694 μm), which can also cover the O + E +

S + C + L + U band. In conclusion, when the error range of t is set to ± 1 nm, the total SB of the proposed SS-DC-PCF PBS changes slightly, even the narrowest total SB can meet the design and engineering requirements. This means that the proposed SS-DC-PCF PBS has a good ETR . The comparisons between the proposed SS-DC-PCF PBS and reported DC-PCF PBS are shown in Table 4. From Table 4, only the SL of Ref [18] is slightly shorter than that of this work, and the proposed PBS has ultra-wide total SB , ultra-low IL , and simple structure. Thus, the proposed SS-DC-PCF PBS has better overall performances.

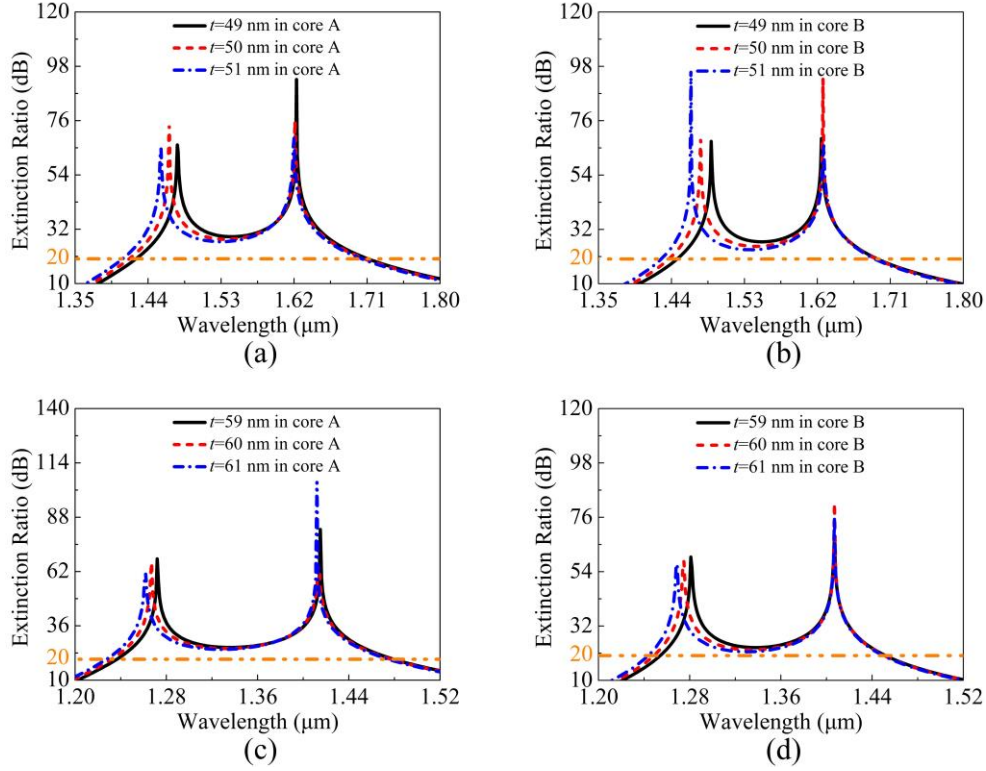


Fig. 15. The ERs in the cores A and B of the proposed (a and b) SS-DC-PCF-1 PBS and (c and d) SS-DC-PCF-2 PBS as functions of the wavelength when t is 49, 50, and 51 μm , and 59, 60, and 61 μm , respectively.

Table 3. The SBs in the cores A and B of the proposed SS-DC-PCF-1 PBS ($SL=176 \mu\text{m}$) and SS-DC-PCF-2 PBS ($SL = 232 \mu\text{m}$) when t is 49, 50, and 51 μm , and 59, 60, and 61 μm , respectively.

SS-DC-PCF-1 PBS, $SL = 176 \mu\text{m}$			SS-DC-PCF-2 PBS, $SL = 232 \mu\text{m}$		
t (nm)	SB in core A (μm)	SB in core B (μm)	t (nm)	SB in core A (μm)	SB in core B (μm)
49	1.426 ~ 1.711	1.447 ~ 1.694	59	1.237 ~ 1.479	1.255 ~ 1.451
50	1.417 ~ 1.707	1.437 ~ 1.692	60	1.232 ~ 1.467	1.249 ~ 1.450
51	1.409 ~ 1.703	1.428 ~ 1.690	61	1.228 ~ 1.474	1.244 ~ 1.449

Table 4. Comparisons between the proposed SS-DC-PCF PBS and reported DC-PCF PBS.

Ref.	DC-PCF structure	Total SB	SL	Max IL
[9]	Hexagonal lattice with two elliptical air holes and two gold wires	S + C + L + U bands	254.6 μm	N/A
[18]	Compressed hexagonal lattice with three kind of circular air holes and liquid crystal	E + S + C + L bands	175 μm	N/A
[19]	Hexagonal lattice with one kind of circular air holes and two gold wires	O and C bands	1.746 mm	N/A
[20]	Hexagonal lattice with two kind of circular air holes and one gold wire	O and C bands	830 μm	N/A
[22]	Diamond lattice with two kind of circular air holes and As_2S_3 layer	S + C + L bands	1 mm	1.1 dB
[23]	Hexagonal lattice with two kind of circular air holes and two gold wires	C band	1.89 mm	N/A
This work	Hexagonal lattice with one kind of circular air holes and one gold film	O + E + S + C + L + U bands	176 μm 232 μm	0.042 dB

4. Conclusions

In summary, a SPR effect-based SS-DC-PCF PBS is proposed. The relationships between the CL and CLR of the SS-DC-PCF-1 PBS and wavelength are investigated by using the symmetric dual-core coupling mode theory. Only the X-pol light exists in the core A and Y-pol light exists in the core B at the three selected wavelengths 1.434, 1.451, and 1.469 μm . The ERs in the cores A and B and corresponding SBs when the SL is equal to 170, 173, and 176 μm are compared. The optimal SL and SB are 176 μm and 255 nm (1.437 ~ 1.692 μm), respectively, and the maximum IL is 0.043 dB. The influences of the change of the structure parameters on the CLs and CLR are also analyzed. The final SL and SB of the SS-DC-PCF-2 PBS are 232 μm and 201 nm (1.249 ~ 1.450 μm), respectively, and the maximum IL is 0.042 dB. The total SB of the proposed SS-DC-PCF-1 PBS and SS-DC-PCF-2 PBS is 443 nm (1.249 ~ 1.692 μm), which can cover the O + E + S + C + L + U band (1.260 ~ 1.675 μm). The total SB of the proposed SS-DC-PCF PBS can always cover the whole optical communication bands when the error range of t is set to ± 1 nm. The proposed SS-DC-PCF PBS has the ultra-short L_s , ultra-wide SB , ultra-low IL , and good ETR , so it can be applied in the all-fiber optical systems.

Funding

National Key Research and Development Project of China (2019YFB2204001).

Acknowledgements

We thank the State Key Laboratory of Information Photonics and Optical Communications (Beijing University of Posts and Telecommunications of China) for the scientific helps and supports throughout this research.

Disclosures

The authors declare no conflicts of interest.

References

1. X. Y. Liu, D. J. Liu, and D. X. Dai, "Silicon polarization beam splitter at the 2 μm wavelength band by using a bent directional coupler assisted with a nano-slot waveguide," *Opt. Express* **29**(2) 2720-2726 (2021).
2. H. I. Stawska, and M. A. Popena, "Fluorescence anisotropy sensor comprising a dual hollow-core antiresonant fiber polarization beam splitter," *Sensors* **20** 3321 (2020).
3. E. Heemskerck, and B. I. Akca, "On-chip polarization beam splitter design for optical coherence tomography," *Opt. Express* **26**(25) 33349-33355 (2018).
4. R. L. Zhou, Q. Li, H. Y. Fu, and K. Nakkeeran, "Quasi-coherent noise-like pulses in a mode-locked fiber laser with a 3D rotatable polarization beam splitter," *Opt. Lett.* **46**(6) 1305-1308 (2021).
5. L. Fang, and J. Wang, "All-fiber polarization beam splitting and rotating based on vector-mode-assisted coupling," *Opt. Express* **26**(12) 15124-15137 (2018).
6. C. Liu, L. Yang, X. L. Lu, Q. Liu, F. M. Wang, J. W. Lv, T. Sun, H. W. Mu, and P. K. Chu, "Mid-infrared surface plasmon resonance sensor based on photonic crystal fibers," *Opt. Express* **25**(13) 14227-14237 (2017).
7. W. C. Zhou, K. W. Li, Y. L. Wei, P. Hao, M. B. Chi, Y. S. Liu, and Y. H. Wu, "Ultrasensitive label-free optical microfiber coupler biosensor for detection of cardiac troponin I based on interference turning point effect," *Biosens. Bioelectron.* **106** 99-104 (2018).
8. L. H. Chu, M. Liu, P. Shum, and Y. B. Fu, "Simultaneous achievement of an ultrashort length and a high extinction ratio polarization splitter based on the dual-core photonic crystal fiber with $\text{Ge}_{20}\text{Sb}_{15}\text{Se}_{65}$ glass," *Appl. Opt.* **58**(28) 7892-7896 (2019).
9. A. Khaleque, and H. T. Hattori, "Ultra-broadband and compact polarization splitter based on gold filled dual-core photonic crystal fiber," *J. Appl. Phys.* **118** 143101 (2015).
10. J. Koo, J. Park, Y. W. Song, S. Lee, K. Lee, and J. H. Lee, "Fiber optic polarization beam splitter using a reduced graphene oxide-based interlayer," *Opt. Mater.* **46** 324-328 (2015).
11. V. Hahn, S. Kal, G. M. Sridharan, M. Wegener, and S. Bhattacharya, "Polarizing beam splitter integrated onto an optical fiber facet," *Opt. Express* **26**(25) 33148-33157 (2018).
12. S. Zhu, Y. Liu, L. Shi, X. B. Xu, S. X. Yuan, N. Y. Liu, and X. L. Zhang, "Tunable polarization beam splitter based on optofluidic ring resonator," *Opt. Express* **24**(15) 17511-17521 (2016).
13. X. B. Zhou, M. W. Qiu, Y. H. Qian, M. M. Chen, Z. X. Zhang, and L. Zhang, "Microfiber-based polarization beam splitter and its application for passively mode-locked all-fiber laser," *IEEE J. Sel. Top. Quantum Electron.* **27**(2) 1-1 (2020).
14. C. B. Ren, J. H. Yuan, K. R. Wang, B. B. Yan, X. Z. Sang, and C. X. Yu, "Design of polarization beam Splitter based on dual-core photonic crystal fiber with three layers of elliptical air holes," *Opt. Eng.* **60**(1) 017102 (2021).
15. B. M. Younis, A. M. Heikal, M. F. O. Hameed, and S. S. A. Obayya, "Highly wavelength-selective asymmetric dual-core liquid photonic crystal fiber polarization splitter," *J. Opt. Soc. Am. B* **35**(5) 1020-1028 (2018).
16. W. L. Lu, S. Q. Lou, X. Wang, L. W. Wang, and R. J. Feng, "Ultrabroadband polarization splitter based on three-core photonic crystal fibers," *Appl. Opt.* **52**(3) 449-455 (2013).
17. T. T. Zhao, S. Q. Lou, X. Wang, M. Zhou, and Z. G. Lian, "Ultrabroadband polarization splitter based on three-core photonic crystal fiber with a modulation core," *Appl. Opt.* **55**(23) 6428-6434 (2016).
18. H. L. Chen, S. G. Li, Z. K. Fan, G. W. An, J. S. Li, and Y. Han, "A novel polarization splitter based on dual-core photonic crystal fiber with a liquid crystal modulation core," *IEEE Photon. J.* **6**(4) 2201109 (2014).
19. Z. K. Fan, S. G. Li, Y. Q. Fan, W. Zhang, G. W. An, and Y. J. Bao, "Designing analysis of the polarization beam splitter in two communication bands based on a gold-filled dual-core photonic crystal fiber," *Chin. Phys. B* **23**(9) 094212 (2014).
20. C. Jimenez-Durango, E. Reyes-Vera, and N. Gomez-Cardona, "Ultra-short polarization beam splitter to operate in two communication bands based on a gold-filled dual-core photonic crystal fiber." in the Latin America Optics and Photonics Conference Tu4A.16 (2018).
21. X. T. Zhao, L. Hua, Q. Xiong, G. H. Jiang, and J. R. Cheng, "Ultra-short and broadband polarization splitter based on PCF and metal surface plasmons resonance," *Opt. Quant. Electron.* **51** 162 (2019).
22. N. Chen, X. D. Zhang, X. L. Lu, Z. Zhang, Z. J. Mu, and M. Chang, "Numerical investigation of a short polarization beam splitter based on dual-core photonic crystal fiber with As_2S_3 layer," *Micromachines* **11** 706 (2020).
23. N. Gomez-Cardona, C. Jimenez-Durango, J. Usuga-Restrepo, P. Torres, and E. Reyes-Vera, "Thermo-optically tunable polarization beam splitter based on selectively gold-filled dual-core photonic crystal fiber with integrated electrodes," *Opt. Quant. Electron.* **53** 68 (2021).
24. Y. W. Qu, J. H. Yuan, X. Zhou, F. Li, B. B. Yan, Q. Wu, K. R. Wang, X. Z. Sang, K. P. Long, and C. X. Yu, "Mid-infrared silicon photonic crystal fiber polarization filter based on surface plasmon resonance effect," *Opt. Commun.* **463** 125387 (2020).
25. X. X. Feng, H. J. Du, S. G. Li, Y. N. Zhang, Q. Liu, and X. Y. Gao, "A polarization filter based on photonic crystal fiber with symmetry around gold-coated holes," *Plasmonics* **13** 1271-1278 (2018).
26. F. C. Meng, X. T. Zhao, J. M. Ding, Y. L. Niu, X. H. Zhang, M. Smietana, R. Buczynski, B. Lin, G. M. Tao, L. Y. Yang, X. Wang, S. Q. Lou, X. Z. Sheng, and S. Liang, "Use of machine learning to efficiently predict the confinement loss in anti-resonant hollow-core fiber," *Opt. Lett.* **46**(6) 1454-1457 (2021).

27. C. Liu, J. W. Wang, F. M. Wang, W. Q. Su, L. Yang, J. W. Lv, G. L. Fu, X. L. Li, Q. Liu, T. Sun, and P. K. Chu, "Surface plasmon resonance (SPR) infrared sensor based on D-shape photonic crystal fibers with ITO coatings," *Opt. Commun.* **464** 125496 (2020).
28. Y. J. Wang, S. G. Li, J. S. Li, Y. Guo, and M. Y. Wang, "Novel external gold-coated side-leakage photonic crystal fiber for tunable broadband polarization filter," *J. Lightw. Technol.* **39**(6) 1791-1799 (2021).
29. Y. J. Wang, S. G. Li, M. Y. Wang, and P. T. Yu, "Refractive index sensing and filtering characteristics of side-polished and gold-coated photonic crystal fiber with a offset core," *Opt. Laser Technol.* **136** 106759 (2021).
30. S. Qiu, J. H. Yuan, X. Zhou, Y. W. Qu, B. B. Yan, Q. Wu, K. R. Wang, X. Z. Sang, K. P. Long, and C. X. Yu, "Highly sensitive temperature sensing based on all-solid cladding dual-core photonic crystal fiber filled with the toluene and ethanol," *Opt. Commun.* **477** 126357 (2020).
31. Q. Liu, S. G. Li, X. Y. Gao, and X. X. Feng, "Simulation of a short and broadband polarization splitter based on photonic crystal fiber filled with tellurite glass," *Opt. Quant. Electron.* **49** 60 (2017).
32. Y. W. Qu, J. H. Yuan, X. Zhou, F. Li, B. B. Yan, Q. Wu, K. R. Wang, X. Z. Sang, K. P. Long, and C. X. Yu, "Surface plasmon resonance-based silicon dual-core photonic crystal fiber polarization beam splitter at the mid-infrared spectral region," *J. Opt. Soc. Am. B* **37**(8) 2221-2230 (2020).
33. V. Kumar, R. K. Varshney, and S. Kumar, "Design of a compact and broadband terahertz polarization splitter based on gradient dual-core photonic crystal fiber," *Appl. Opt.* **59**(7) 1974-1979 (2020).
34. L. H. Jiang, Y. Zheng, L. T. Hou, K. Zheng, J. Y. Peng, and X. T. Zhao, "An ultrabroadband polarization splitter based on square-lattice dual-core photonic crystal fiber with a gold wire," *Opt. Commun.* **351** 50-56 (2015).
35. H. L. Chen, S. G. Li, G. W. An, J. S. Li, Z. K. Fan, and Y. Han, "Polarization splitter based on d-shaped dual-core photonic crystal fibers with gold film," *Plasmonics* **10** 57-61 (2015).
36. Y. W. Qu, J. H. Yuan, S. Qiu, X. Zhou, F. Li, B. B. Yan, Q. Wu, K. R. Wang, X. Z. Sang, K. P. Long, and C. X. Yu, "A novel gold film-coated v-shape dual-core photonic crystal fiber polarization beam splitter covering the E + S + C + L + U band," *Sensors* **21** 496 (2021).
37. J. C. Knight, J. Broeng, T. A. Birks, P. St. J. Russell, "Photonic Band Gap Guidance in Optical Fibers," *Science* **282** 476-478 (1998).
38. Y. Li, K. Itoh, W. Watanabe, K. Yamada, D. Kuroda, J. Nishii, and Y. Y. Jiang, "Three-dimensional hole drilling of silica glass from the rear surface with femtosecond laser pulses," *Opt. Lett.* **26**(23) 1912-1914 (2001).
39. A. Bertoncini, and C. Liberale, "3D printed waveguides based on photonic crystal fiber designs for complex fiber-end photonic devices," *Optica* **7**(11) 1487-1494 (2020).
40. X. Feng, A. K. Mairaj, D. W. Hewak, and T. M. Monro, "Nonsilica glasses for holey fibers," *J. Lightw. Technol.* **23**(6) 2046-2054 (2005).
41. P. J. A. Sazio, A. Amezcua-Correa, C. E. Finlayson, J. R. Hayes, T. J. Scheidemante, N. F. Baril, B. R. Jackson, D. J. Won, F. Zhang, E. R. Margine, V. Gopalan, V. H. Crespi, and J. V. Badding, "Microstructured optical fibers as high-pressure microfluidic reactors," *Science* **311** 1583-1586 (2006).
42. J. Boehm, A. François, H. Ebendorff-Heidepriem, and T. M. Monro, "Chemical deposition of silver for the fabrication of surface plasmon microstructured optical fibre sensors," *Plasmonics* **6** 133-136 (2011).
43. B. Y. Li, Z. C. Sheng, M. Wu, X. Y. Liu, G. Y. Zhou, J. T. Liu, Z. Y. Hou, and C. M. Xia, "Sensitive real-time monitoring of refractive indices and components using a microstructure optical fiber microfluidic sensor," *Opt. Lett.* **43**(20) 5070-5073 (2018).
44. D. J. J. Hu, and H. P. Ho, "Recent advances in plasmonic photonic crystal fibers: design, fabrication and applications," *Adv. Opt. Photonics* **9**(2) 257-314 (2017).